Journal of Neural Engineering

PURPOSE-LED PUBLISHING™

PAPER • OPEN ACCESS

NeuroNella: Automatic identification of neural activity from multielectrode arrays with blind source separation

To cite this article: C Germer *et al* 2025 *J. Neural Eng.* **22** 026059

View the article online for updates and enhancements.

You may also like

- Biomimetic stimulation patterns drive natural artificial touch percepts using intracortical microstimulation in humans
Taylor G Hobbs, Charles M Greenspon, Ceci Verbaarschot et al.
- Fascicle-selective kilohertz-frequency neural conduction block with longitudinal intrafascicular electrodes
Louis Regnacq, Anil K Thota, Arianna Ortega Sanabria et al.
- Navigational outcomes with a depth-based vision processing algorithm in a second-generation suprachoroidal retinal prosthesis
Lauren Moussallem, Lisa Lombardi, Myra B McGuinness et al.

This content was downloaded from IP address 155.198.12.188 on 25/06/2025 at 11:44

Journal of Neural Engineering

OPEN ACCESS

RECEIVED
9 September 2024

REVISED
20 February 2025

ACCEPTED FOR PUBLICATION
26 March 2025

PUBLISHED
16 April 2025

Original content from this work may be used under the terms of the Creative Commons Attribution 4.0 licence.

Any further distribution of this work must maintain attribution to the author(s) and the title of the work, journal citation and DOI.

PAPER

NeuroNella: Automatic identification of neural activity from multielectrode arrays with blind source separation

C Germer[1,2], D Farina[3], S N Baker[4] and A Del Vecchio[5,*]

[1] Departamento de Eletrônica e Engenharia Biomédica, Faculdade de Engenharia Elétrica e de Computação, Universidade Estadual de Campinas, Campinas, Brazil
[2] Neural Engineering Research Laboratory, Centro de Engenharia Biomédica, Universidade Estadual de Campinas, Campinas, Brazil
[3] Department of Bioengineering, Imperial College London, London, United Kingdom
[4] Faculty of Medical Sciences, Newcastle University, Newcastle upon Tyne, United Kingdom
[5] Department of Artificial Intelligence in Biomedical Engineering, Friedrich-Alexander University Erlangen-Nürnberg, Erlangen, Germany
[*] Author to whom any correspondence should be addressed.

E-mail: alessandro.del.vecchio@fau.de

Keywords: independent component analysis, extracellular decomposition, neural activity

Supplementary material for this article is available online

Abstract

Objective. The identification of individual neuronal activity from multielectrode arrays poses significant challenges, including handling data from numerous electrodes, resolving overlapping action potentials and tracking activity across long recordings. This study introduces NeuroNella, an automated algorithm developed to address these challenges. *Approach.* NeuroNella employs blind source separation to leverage the sparsity of action potentials in multichannel recordings. It was validated using three datasets, including two publicly available ones: (1) *in vitro* recordings (252 channels) of retinal ganglion cells from mice with simultaneous ground-truth loose patch data to assess accuracy; (2) a Neuropixel recording from an awake mouse, comprising 374 channels spanning different brain areas, to demonstrate scalability with dense multielectrode configurations in *in vivo* recordings; and (3) data (32 channels) recorded from the medullary reticular formation in a terminally anaesthetised macaque, to showcase decomposition over long periods of time. *Main results.* The algorithm exhibited an error rate of less than 1% compared to ground-truth data. It reliably identified individual neurons, detected neuronal activity across a wide amplitude range, and tolerated minor probe shifts, maintaining robustness in prolonged experimental sessions. *Significance.* NeuroNella provides an automated and efficient method for neuronal activity identification. Its adaptability to diverse dataset, species, and recording configurations underscores its potential to advance studies of neuronal dynamics and facilitate real-time neuronal decoding systems.

1. Introduction

Accurate transmission of information allows biological and non-biological systems to interact and communicate with the environment. Communication between and within biological structures is due to the coordinated activity of neural networks in the brain and spinal cord. This communication takes place at the level of individual neurons and populations of neurons and can be investigated from the firing activity of single neural cells, usually identified from multi-unit recordings [1].

Classic invasive electrode systems placed in neural tissues maximize selectivity, i.e. the contribution in signal energy of a few neurons is dominant with respect to the surrounding neuronal activities [2–5]. The advent of novel technologies, such as complementary metal oxide semiconductor (CMOS) sensors [6, 7], allows the fabrication of thousands of closely-spaced electrodes; each electrode can record action potentials from multiple neural sources. Because of the increase in signal complexity, more complex algorithms with respect to classic clustering methods have been proposed [8–10] to identify these neural

© 2025 The Author(s). Published by IOP Publishing Ltd

ensembles. Yet, most of the current software still relies on conventional spike sorting approaches [7, 8, 11], with newer methods incorporating convolutional network and deep learning techniques [9, 10, 12, 13]. Spike sorting algorithms are classically based on segmentation and classification. This scheme assumes that the probability of action potentials overlapping over time is relatively low. When action potentials overlap in the same time interval, however, the identification of their waveforms and therefore the association to specific neurons is challenging. Overlapping of action potentials rapidly increases with decreasing selectivity. A theoretical approximation [14] indicates that the number of overlapped action potentials per unit time (Ov) depends on the number of active detected neurons (N), their average firing frequency (f), and the action potential waveform duration (d), according to the relation $Ov = f^2 dN$. As the number of detected neurons increases, the overlap rate increases linearly. For example, for 2 detected neurons, with an average firing at 50 Hz, and action potential duration of 1 ms, the average overlap rate would be only 5 action potentials/s, but when the number of detected neurons slightly increases to 10 the overlap rate increases to 25 action potentials/s. Therefore, overlapping of action potentials in time becomes a major challenge as soon as the selectivity of each electrode is slightly reduced. Conventional spike sorting approaches that segment the recording in time intervals containing action potential waveforms and cluster the segmented waveforms, without resolving action potentials overlapped in time, can only be applied with very selective electrodes. Attempts to identify overlapped potentials require complex calculations; these may not be feasible if there is a need for online sorting.

CMOS sensor technology opened up a new way of extracting neural data due to the high density of the electrodes and the fact that each electrode records multiple sources. Because of the rich information recorded by these systems, conventional spike sorting fails in providing accurate identification of all neural firings. While new methods based on source separation have been proposed for neural decoding [15], none of the current methods leverages the main characteristics of the neuronal sources, i.e., their *spatiotemporal sparsity*. Temporal sparsity is a strong prior that is valid for any recording from neural (and muscular) tissues [16, 17]. It is due to the fact that the sources to be identified can be modeled by Dirac delta functions with a certain probability of occurrence over time (temporal sparsity) and a local distribution in space (spatial sparsity).

Here we propose a blind source separation approach for decoding neural signals. The method adapts validated algorithms previously applied in the decomposition of high-density electromyography (HD-sEMG) [17–19] and tailors them to address the unique challenges of invasive multielectrode dense arrays [13]. These challenges include managing large datasets resulting from high electrode counts and sampling rate, long-duration recordings, electrode drift, and poor spatial resolution. Unlike conventional spike sorting, our approach is solely based on the assumption that the sources to be decoded are sparse in both time and space, enabling the separation of neural activity without being influenced by the action potential overlap rate and without any further *a-priori* assumptions on the statistics of neural activity. We demonstrate that a blind iterative update procedure that maximizes the sparsity of each estimated source allows the identification of action potential firing times, as long as each action potential waveform is unique in space-time. Importantly, the method was extensively validated on data from concurrent recordings of neuronal action potentials by loose patch and multielectrode arrays. We analyzed data from different anatomical structures ranging from the mice retina to the brainstem of anesthetized macaques. Our results show that the proposed method is highly reliable in providing robust and accurate results.

2. Methods

2.1. Details of the algorithm

In this section, we provide an overview of the algorithm's general framework, followed by a detailed explanation of the steps involved in the blind source separation algorithm for extracellular recording. These steps include: (i) the spatial segmentation procedure to optimize the decomposition of dense probes; (ii) the data representation of electrophysiological recording as an instantaneous convolutive mixture model [16–18, 20, 21]; (iii) the theoretical basis for the separation algorithm, which combines independent component analysis [22], fast independent component analysis (fastICA [18, 23, 24]), convolutive blind source separation algorithm [17] and the peel-off procedure [19]; (iv) the description of a classification algorithm to improve selection of spike instances; and (v) the procedure to extend the decomposition to long recordings.

2.1.1. General overview

NeuroNella is a fully automatic algorithm that blindly identifies sources from multielectrode extracellular recordings. Instead of classification based on the waveform shape, NeuroNella separates action potentials by spatio-temporal filters that maximize the sparsity of the estimated sources. Due to the confinement of the neuron activity in a few neighboring electrodes (spatial sparsity), the algorithm starts by spatial segmentation of the dense probe into smaller sub-groups of channels to reduce the computational

burden and to increase the probability of identification of sources with small signal amplitude. This classification algorithm clusters the channels into sub-groups with N desired channels, taking into account the signal energy (root-mean-square) and location in the probe. It therefore provides sub-groups with similar number of channels, but with different geometry (figure 1). Each sub-group of neighboring electrodes contains the spatial distribution of one or more neuronal activities. Segments of 25 channels have provided a good trade-off of total processing time and number of identified sources in our tests, although this parameter can be varied depending on the application. The algorithm proceeds to the decomposition of some or all spatial segments of the probe, starting with sub-groups with higher energy, as this indicates those most likely to contain neuronal activity.

For each spatial segment, virtual channels are created as temporally-delayed versions of each observation (step 2 in figure 1(a)). The original sources (i.e. neuronal activities) are estimated by first whitening the extended observations and then rotating them by projecting the whitened observation into a separation vector. The aim of the algorithm is to blindly estimate the separation vector of each source. For each new source to be estimated, a separation vector is initialized on the location of a detected spike (with peak detection, step 3 in figure 1(a)). The separation vector is updated iteratively with a fixed-point algorithm until convergence. The central limit theorem states that summation of sources is always more Gaussian (and indirectly less sparse) than the individual sources, thus, the criterion for the fixed-point algorithm is to maximize the temporal sparsity of the estimated sources, measured by the kurtosis ($G = s^3/3$, where s is the estimated discharge train and G the cost function). This criterion suffices to separate the sources due to the intrinsic structure of the firing trains (most samples are zero) and the high sampling frequency of the extracellular recording. The estimated source is retrieved with a one-step matrix multiplication of the separation vector and the extended matrix of observation. The process is insensitive to overlapping action potentials, except for the case of action potentials with identical spatio-temporal waveforms, which are indistinguishable. To facilitate the detection of the peaks, the estimated source is raised to the power of three, yielding the estimated series of discharges (discharge train). A classification algorithm then evaluates each peak detected in the estimated discharge train with the respective amplitudes in representative extracellular signals to improve accuracy on the selection of the discharge instants (figure 1(b)). A pulse-to-noise ratio (PNR) [25] is calculated on the estimated discharge train, and if the index crosses a defined threshold (25 dB), the source is confirmed, otherwise it is discarded. The PNR measures the quality of the decomposition and is an indicator of accuracy of the discharge instants identification. After identification of some sources, a peel-off procedure is applied to derive a residual signal to which the same algorithm is applied.

2.1.2. Segmentation of dense probes

The activity of single neurons is spatially sparse because of the spatial selectivity of the multielectrode systems. When identifying a source, the observations that do not register the source activity unnecessary increase the computational cost and noise. Segmentation into sub-groups of channels is therefore crucial for large probes. In cases of more than 40 channels, we segment the probe into sub-groups of neighboring electrodes with similar signal energy (root-mean-square). For this, a K-means++ algorithm uses the energy recorded in each electrode and its location in the probe (X and Y) to segment it into N non-overlapping sub-groups. The number of segments (N classes) depends on the electrode density in the probe, but generally aims at having about 25 channels per sub-groups. It should be noted that the source can still be identified even when its spatial distribution is divided into two or more sub-groups, provided it has a unique spatio-temporal distribution, and a significant signal energy compared to other sources. Nonetheless, decomposition of overlapped segments may alleviate potential subdivision effects. In both cases, duplicity in the source identification may occur, but can be easily eliminated in subsequent steps.

2.1.3. Data model and separation background

The problem we want to address is the blind identification of neuronal activities extracted from electrophysiological recordings. This can be modeled as a classic cocktail-party problem, where the intent is to retrieve the speech signals of multiple speakers who are simultaneously talking in a room with multiple microphones. The speech signal is filtered by the acoustic properties of the environment before reaching each microphone, yielding a unique spatial distribution of each speech. Likewise, the electrophysiological signals recorded by implanted electrodes in brain tissue are the filtered versions of the action potential trains of multiple neurons.

The electrophysiological data can be modeled as an instantaneous convolutive mixture, as it consists of the convolutional combination of action potential waveform and the discharge times. Assuming the source signals arrive at the sensors at the same time, the model is also said to be instantaneous. The same model is found in the case of invasive and non-invasive HD-EMG, extensively described elsewhere [16–18]. The observations (channels) comprise the summation of action potential trains, for which the waveform is considered invariant in time and specific

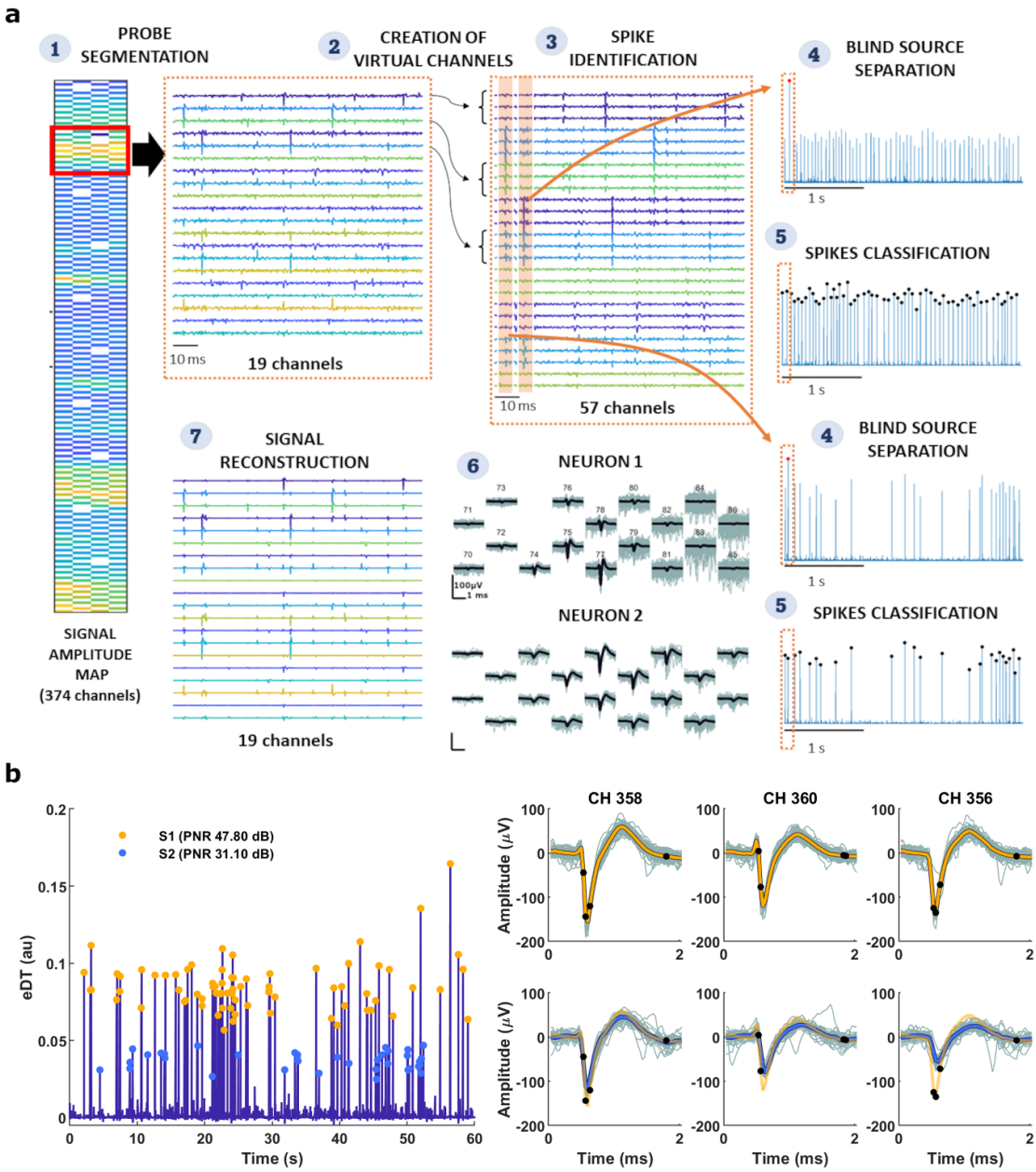

Figure 1. (a) Main steps of the decomposition algorithm. Step 1, the dense probe is segmented into subgroups according to the signal energy (root-mean-squared) and location. The amplitude map shows the energy of each channel (color coded), the probe's geometry, and the segmentation (red polygon). The panel on the right shows the recorded signals for the selected channels. Each line represents one channel. Step 2, virtual channels are created as delayed versions of the original data. The extension factor is 3 for clarity and graphical purposes but was usually >6 (refer to section Data Model and Separation Background for additional details). Step 3, a peak detection algorithm locates a spike instant and initializes a separation vector for the fixed-point algorithm. Step 4, the blind source separation algorithm computes the estimated discharge train by a simple multiplication of the separation vector and the extended observations and enhances the peaks by powering to three. Step 5, the algorithm converges to the estimated source in a few iterations from which the discharge instants are recovered by a peak detection algorithm. Steps 3–5 are repeated N times chosen by the user. For each iteration, the algorithm can converge to a new source, an already identified source, or a non-physiological source (noise). The non-physiological and repeated sources are discarded. Step 6, the signal waveforms of each source are estimated by a spike-triggered average and the activity of all sources is summed to give the reconstructed signal (Step 7). Steps 2–7 are repeated for the residual signal obtained after extraction of the reconstructed signal from the original observations (peel-off procedure). The entire process is performed at each segment of the probe. (b) Representative process for peak classification in a noisy estimated discharge train (eDT). The classification algorithm distinguishes two sources by analyzing each detected peak in the eDT alongside the corresponding amplitudes in representative extracellular signals. Shimmer plots display the action potentials of source 1 (first row) and source 2 (second row) for the three channels. The averaged action potential of each source is shown in distinct colors (yellow for S1 and blue for S2). Black markers indicate the time points utilized in the classification algorithm.

for the neuron and channel. Assuming N active neurons are recorded by M electrodes, the signal on each channel can be described as:

$$x_m(t) = \sum_{l=0}^{L-1}\sum_{n=1}^{N} a_{nm}(l)\, s_n(t-l) + \eta_m(t),$$
$$m = 1,\ldots,M;\ t = 0,\ldots,D_R \quad (1)$$

where $x_m(t)$ is the observation in the mth channel at the time instant t (in the discrete time), D_R is the duration of the recording (in samples), $a_{nm}(l)$ is the action potential waveform of the nth neuron in the mth channel, L is the length of the action potential waveform, s_n is the discharge train of the nth neuron modeled by a series of Dirac Delta function ($s_n(t) = \sum_k \delta(t - T_n(k))$, where T_n are the discharge instants), and $\eta_m(t)$ is the additive noise at channel m. Due to the refractory period, we can assume no overlapping of action potentials for the same neuron, thus $T_n(k+1) - T_n(k) > L$ for $\forall k \in \mathbb{N}$.

In the vector-matrix notation, equation (1) becomes

$$\boldsymbol{x}(t) = \sum_{l=0}^{L-1} \boldsymbol{A}(l)\, \boldsymbol{s}(t-l) + \boldsymbol{\eta}(t) \in \mathbb{R}^{M\text{x}1} \quad (2)$$

Equation (2) represents a finite impulse response filtering of the sources, where $\boldsymbol{x}(t) = [x_1(t), x_2(t), \ldots, x_M(t)]^T$ is the vector of observations, $\boldsymbol{A}(l) = [\boldsymbol{a}_1(l), \ldots, \boldsymbol{a_N}(l)]$ is the action potential filter of order L and size $M \times N$, and $\boldsymbol{s}(t) = [s_1(t), \ldots, s_N(t)]^T$ is the vector of sources at time instant t. Superscript T denotes transposition of a vector or a matrix.

The model (2) can be further represented in matrix form, containing the latest L samples of the sources [16–18]. In this way, the new vector of sources become:

$$\underline{\boldsymbol{s}}(\boldsymbol{t}) = \left[\boldsymbol{s}^T(t), \boldsymbol{s}^T(t-1), \ldots, \boldsymbol{s}^T(t-L+1)\right]^T \in \mathbb{R}^{NL\text{x}1}.$$

In order to improve the ratio between the number of observations and sources, the observations are also extended by $K-1$ delayed versions, here after referred to as the extension factor

$$\tilde{\boldsymbol{x}}(t) = \tilde{\boldsymbol{A}}\tilde{\boldsymbol{s}}(t) + \tilde{\boldsymbol{\eta}}(t). \quad (3)$$

Which is represented by a block-based model that represents the extended vector of observations containing the original signals and its delayed versions [23].

With:

$$\tilde{\boldsymbol{x}}(t) = [\tilde{\boldsymbol{x}}_1, \tilde{\boldsymbol{x}}_2, \ldots, \tilde{\boldsymbol{x}}_{\boldsymbol{M}}]^T \in \mathbb{R}^{MK\text{x}1}$$
$$\tilde{\boldsymbol{x}}_{\boldsymbol{m}}(t) = [x_m(t), x_m(t-1), \ldots, x_m(t-K+1)],$$
$$m = 1, \ldots, M$$
$$\tilde{\boldsymbol{\eta}}(t) = [\tilde{\boldsymbol{\eta}}_1, \tilde{\boldsymbol{\eta}}_2, \ldots, \tilde{\boldsymbol{\eta}}_{\boldsymbol{N}}]^T \in \mathbb{R}^{MK\text{x}1}$$
$$\tilde{\boldsymbol{\eta}}_{\boldsymbol{m}}(t) = [\eta_m(t), \eta_m(t-1), \ldots, \eta_m(t-K+1)],$$
$$m = 1, \ldots, M$$
$$\tilde{\boldsymbol{s}}(t) = [\tilde{\boldsymbol{s}}_1, \tilde{\boldsymbol{s}}_2, \ldots, \tilde{\boldsymbol{s}}_{\boldsymbol{N}}]^T \in \mathbb{R}^{N(L+K)\text{x}1}$$
$$\tilde{\boldsymbol{s}}_{\boldsymbol{n}}(t) = [s_n(t), s_n(t-1), \ldots, s_n(t-L-K+2)],$$
$$n = 1, \ldots, N$$

$$\tilde{\boldsymbol{A}} = \begin{bmatrix} \tilde{\boldsymbol{A}}_{11} & \cdots & \tilde{\boldsymbol{A}}_{1\text{N}} \\ \vdots & \ddots & \vdots \\ \tilde{\boldsymbol{A}}_{1\text{M}} & \cdots & \tilde{\boldsymbol{A}}_{\text{MN}} \end{bmatrix} \in \mathbb{R}^{MK\text{x}N(L+K)}$$

$$\tilde{\boldsymbol{A}}_{mn} = \begin{bmatrix} a_{mn}(0) & a_{mn}(1) & \ldots & a_{mn}(L-1) & 0 & \ldots & 0 \\ 0 & a_{mn}(0) & \ldots & a_{mn}(L-2) & a_{mn}(L-1) & \ldots & 0 \\ \vdots & \ddots & \ddots & \ddots & \ddots & \ddots & \vdots \\ 0 & \ldots & 0 & a_{mn}(0) & \ldots & a_{mn}(L-2) & a_{mn}(L-1) \end{bmatrix}.$$

The sources can be retrieved by estimating a demixing matrix $\tilde{\boldsymbol{D}}$:

$$\widehat{\tilde{\boldsymbol{s}}}(t) = \tilde{\boldsymbol{D}}\tilde{\boldsymbol{x}}(t) \quad (4)$$

where $\tilde{\boldsymbol{D}} \in \mathbb{R}^{N(L+K)\text{x}MK}$ is the matrix of coefficients of the separating system filters, also called matrix of weights, and $\widehat{\tilde{\boldsymbol{s}}}(t)$ is the estimated source vector. The demixing problem builds on the fundamental assumption of statistical independence or sparseness (non-Gaussianity) of the sources. The model also assumes that the source signal vector are zero-mean stationary real signals and is independent of the noise vector. To make the zero-mean assumption hold we center the observation matrix by subtracting their sample mean. Moreover, the extension factor (K) should be large enough to assure $MK \geq N(L+K)$ to yield to an overdetermined multiple-input multiple-output demixing model. One must account for the dimension growth of the problem when the extension factor and/or the number of channels (M) are

too large, especially for recordings with high sampling frequency (20 kHz) and long duration, as it leads to prohibitively high dimensions and computation overload. An extension factor $K = 300/M$ was used, where M is the number of channels per sub-group of the probe.

Once the convolutive mixture model (equation (1)) is approximated to an instantaneous linear mixture model (equation (3)), we can proceed to the separation problem by standard linear independent component analysis. The approach chosen was fastICA [23], as it has been successfully applied and validated for HD-sEMG [18].

The zero-mean extended observations are spatially whitened, such that the channels are mutually uncorrelated and have unit variance. To ensure stability, a regularization factor equal to the 20th percentile of the eigenvalues was used. After the transformation, and omitting the noise for simplicity, it gives

$$\boldsymbol{z}(t) = \boldsymbol{W}\tilde{\boldsymbol{x}}(t) = \boldsymbol{W}\tilde{\boldsymbol{A}}\tilde{\boldsymbol{s}}(t) = \boldsymbol{B}\tilde{\boldsymbol{s}}(t) \tag{5}$$

where $\boldsymbol{W}$ is the whitening matrix, and $\boldsymbol{B}$ is an orthogonal matrix owing to the assumption of sparse sources. The demixing model is then given by

$$\hat{\tilde{\boldsymbol{s}}}(t) = \boldsymbol{B}^T\boldsymbol{z}(t)\,. \tag{6}$$

Equation (6) holds that source separation is achieved based on the estimation of a separation matrix $\boldsymbol{B}$. This matrix is found by an iterative procedure (fastICA) that optimizes a contrast function chosen based on the statistical properties of the neuronal discharge trains: its intrinsically sparse distribution (most samples are zeros), closely related to supergaussianity. According to the central limit theorem, the sum of non-Gaussian random variables is closer to Gaussian than the original ones. Therefore, each source of equation (6) ($\hat{s}_i = b^T\boldsymbol{z}$) can be iteratively estimated by finding the vector b that maximizes the non-Gaussianity of $b^T\boldsymbol{z}$. Estimates representative for the statistical properties of the source and related to non-Gaussianity can be used as contrast functions, such as kurtosis and skewness given by $G(s) = s^4/4$, and $G(s) = s^3/3$, respectively [24, 26]. The separation vector is optimized iteratively by a fixed-point algorithm given by [23]:

$$b_{\text{new}} = E\left\{\boldsymbol{z}G\left(b_{\text{old}}^T\boldsymbol{z}\right)\right\} - E\left\{G'\left(b_{\text{old}}^T\boldsymbol{z}\right)\right\}b \tag{7}$$

where E stands for mathematical expectation. Normalization of the separation vector to unit norm is necessary at each iteration to keep the variance of the estimated source constant. This loop runs until there is no significant changes in the separation coefficients, such that $\left|b_{\text{new}}^T b_{\text{old}} - 1\right| \leq 10^{-4}$, or up to 30 iterations.

To facilitate the identification of the discharge instants on the estimated source ($\hat{s}_i = b^T\boldsymbol{z}$), we enhance peak prominence by raising the signal to the power of three while preserving polarity, thereby obtaining the so-called estimated discharge train, as follows

$$\text{eDT}_i(t) = \hat{s}_i^3(t)\,. \tag{8}$$

The peaks are then detected by a first-derivative method and classified by a clustering method (see Peak Classification Algorithm section). The quality of the classification of the peaks is evaluated with the modified PNR index [25]

$$\text{PNR}_i = 10\log_{10}\frac{E\left\{\text{eDT}_i(t)\,|_{t\in T_{ni}}\right\}}{E\left\{\text{eDT}_i(t)\,|_{t\notin T_{ni}\,\&\,\text{eDT}_i(t)>0}\right\}} \tag{9}$$

where T_{ni} represents the selected discharge instants of source i. Note that only positive noise are considered in the denominator. PNR indicates accurate peak identification, as high PNR is achieved when the base-line noise levels are low in comparison to the amplitude of the selected peaks. The source was accepted if PNR was greater than a threshold of 25 dB.

We then compute the action potential waveforms of the source for each channel with spike-triggering average of the original recordings, and the entire action potential trains are recovered by convolving the action potential waveforms with the pulse train.

The process described above is the basis for recovering one independent source. For multiple sources, the fixed-point algorithm must be run several times. For every source identified, we check for duplicity and, if false, the separation vector, the discharge instants and the waveforms are stored. Two sources are considered equal if the cross-correlation between the discharge trains normalized by the minimum number of discharges is higher than 0.5, accounting for time shifts of the discharge instants of ± 0.1 ms. When duplicity occurs, the source with the smallest PNR is deleted. To avoid the convergence of the algorithm to sources already found, a deflationary orthogonalization procedure $b_p \leftarrow b_p - \sum_{j=1}^{p}\left(b_p^T b_j\right)b_j$ is added in the loop following the update step (equation (7)) and prior to normalization. Duplicity is also avoided by choosing adequate initialization of the separation vector. A good initialization is the observation vector at the time instant of a detected discharge, thus, $b_0 = \boldsymbol{z}(t_k)$, where $\boldsymbol{z}$ is the whitened extended observations and t_k is the detected time instant [17]. The time instants are chosen based on an activity index, computed as the summation of the squared whitened observations [17], as high values indicate neuronal activity from at least one source recorded by at least one channel. Once the discharge train of a source is identified, the corresponding time instants of the activity index are zeroed, and the maximum value of the activity index sets the initialization vector for the next source.

The fastICA, as any blind source separation algorithm, is limited to extract the sources that most contribute to the signal. To allow extraction of more sources, the peel-off procedure [27] is performed to remove from the original data the action potential trains of the extracted sources, allowing the convergence of the fastICA to less significant sources. This procedure may impose minor estimation errors in the model if repeated, which did not appear to occur here.

In sum, the algorithm behind NeuroNella is to segment the probe into sub-groups and perform two steps of fastICA, one with the original electrophysiological recordings and the other with the residual signal following the peel-off procedure. In each step of fastICA, a set number of iterations determines how many times the algorithm will attempt to extract a source by initializing a separation vector and optimizing it with the fixed-point algorithm. Duplicity of neurons are checked at each step of the fastICA and for adjacent sub-groups.

2.1.4. Peak classification algorithm

Some estimated discharge trains have poor signal-to-noise ratio (SNR) due to similarities in the spatial distribution of nearby neurons. High background noise may lead to misclassification of the discharge times and necessitates further inspection. To overcome this issue, we developed an algorithm to recognize the peaks in a noisy estimated discharge train based on a clustering analysis that accounts both for the amplitude of the peaks and the corresponding amplitude in three extracellular signals closest to the source (taken from the separation vector b).

The algorithm is based on a hierarchical clustering algorithm limited to 20 clusters (function *clusterdata*, from Matlab®). First, the algorithm detects peaks in the estimated discharge train with minimal interval of 1 ms, thereby selecting both signal and noise. Then, the algorithm computes the associated waveforms of each selected time instant by spike-triggering three extracellular signals with a window length of 3 ms. Reference waveforms are derived by averaging only the waveforms corresponding to peaks surpassing a specific threshold, typically set to 0.05% of the second norm of the estimated discharge train.

As an input for the clustering analysis, at each time point, the algorithm calculates the root-mean-square deviation between the associated waveform and the reference waveforms (from the three best extracellular signals) and assesses the waveform amplitude at four critical points: the peak and three points automatically chosen based on their variability among all waveforms (black markers on the waveforms of figure 1(b)). In the final phase, the algorithm arranges the clusters based on the estimated discharge train amplitude's centroid and explores reducing the number of clusters by merging those with similar action potential waveforms to the first cluster under the following conditions: (i) the combined correlation of the action potential across the three extracellular signals exceeds 2.5; (ii) the centroid of the discharge train amplitude surpasses 0.5 of the first cluster's centroid. (iii) The root-mean-square deviation of the action potential for the best extracellular signal falls below 3.

This algorithm is adaptable for semi-automatic use during manual inspection of peek classification. Users can customize various parameters to suit specific datasets and conditions. For instance, the use of *a priori* reference waveforms is particularly valuable for extending decomposition, as it enables leveraging identified discharges in overlapping segments to classify those in unprocessed portions of the signal. When no reference waveform is provided, the algorithm defaults to selecting the cluster with the largest centroid of estimated discharge train amplitude. The number of critical time points in the waveform amplitude is another particularly useful attribute, especially for distinguishing sources with highly similar action potentials across the top three channels. While four points often suffice, fewer or more points may be optimal in certain cases. Additionally, users can adjust the weighting of the attributes input into the cluster analysis. For example, when differences in amplitude within the estimated discharge train are pronounced, assigning a higher weight to this feature can aid in differentiation, similarly to the case shown in figure 1(b). Conversely, when amplitude differences are minimal, reducing its weight may enhance performance. In some cases, increasing the weight for the root-mean-square deviation for a specific channel, such as channel three in figure 1(b), can improve accuracy. Manual editing was required in only one instance for the ground-truth dataset and occasionally during the extension of decomposition to longer recordings, when signals drifts and sudden activation of other neurons are common.

2.1.5. Extension of the decomposition

NeuroNella can run on a computer without GPU, however, the size of the extended observation matrix is a limiting factor. The computational cost is determined by the number of selected channels, the extension factor, the time duration, and the sampling frequency. In this study, decompositions were limited to recording segments ranging from 30 s to 120 s. If a longer decomposition is necessary, the decomposition of one segment can be extended to the next segment of data. To account for minor drifts in the probe and subsequent changes in the action potential waveform and spatial distribution of each source, it is recommended to perform the extension procedure in segments no longer than 60 s of recording, with an

overlap of 50%, and to update the estimation parameters based on the new data. The extension procedure used here is similar to the online decomposition of HD-sEMG described in [28]. A slightly modification of equation (6) allows the retrieval of the estimated discharge train without whitening the new data, as follows [17]:

$$\widehat{\widetilde{s}}_n(t) = \boldsymbol{B}^T \boldsymbol{C}_{\bar{x}\bar{x}}^{-1} \bar{\boldsymbol{x}}_n(t) \tag{10}$$

where $\widehat{\widetilde{s}}_n$ is the estimated sources for the new segment and $C_{\bar{x}\bar{x}}$ stands for the covariance matrix of the extended observations, updated at the covariance matrix of each new segment ($C_{\bar{x}_n\bar{x}_n}$) by equation (11)

$$C_{\bar{x}\bar{x}\text{new}} = C_{\bar{x}\bar{x}\text{old}} + C_{\bar{x}_n\bar{x}_n}. \tag{11}$$

Every separation vector that constitutes the separation matrix ($\boldsymbol{B} = \begin{bmatrix} b_1 & \dots & b_m \end{bmatrix}$) is obtained from the initial decomposed segment, as follows:

$$b_i^0 = \frac{1}{N}\sum_k^N \tilde{\boldsymbol{x}}(t_k) \tag{12}$$

where t_k is the kth discharge time (from 1 to N discharges) of the ith source extracted.

The process of identifying discharge times within the newly estimated discharge train involves the hierarchical clustering analysis (described in 'Peak Classification Algorithm' section) of a data segment that overlaps with the preceding segment. This overlapping segment provides a reference to historical discharge times and action potential waveforms. This process compensates for potential drifts in the recording system and accommodates the activation of new sources, both of which contribute to fluctuations in the amplitude of both signal and noise in the estimated discharge train.

The newly identified discharges are used to update the separation vector, as follows:

$$b_i^{I+1} = \frac{N_{\text{new}} b_i^{\text{new}} + N b_i^I}{N_{\text{new}} + N} \tag{13}$$

where, N_{new} is the number of identified discharges in the new segment, b_i^{new} is the separation vector evaluated within the new segment, and N denotes the cumulative count of identified discharges up to the current segment.

Since the Peak Classification Algorithm can also identify new sources contributing to the estimated discharge train (as seen as Source 2 in figure 1(b)), those exhibiting a PNR greater than 25 dB are stored and subsequently examined in the new segment.

2.2. Experimental recordings and data processing

2.2.1. In vitro *ground-truth in mice retina*

For comparisons with published ground-truth data [29] we applied the proposed algorithm (NeuroNella) to an *in vitro* dataset comprising simultaneous loose patch and dense extracellular recordings (252 electrodes) from retinal ganglion cells in mice, available in an online database [29] and with experimental protocols described elsewhere [8]. The extracellular signals were sampled at 20 kHz and pre-processed using a third-order Butterworth filter with a high-pass cutoff frequency of 100 Hz. We then converted the signals to microvolts by subtracting a predefined offset value (of $2^{15}-1$) and applying a gain factor of 0.1042, following the instructions in [29]. To ensure reliable ground-truth data, recordings with poor patch signal quality were excluded. The exclusion criterion was based on the SNR [30], with recordings having spikes of amplitudes comparable to the noise level considered unsuitable. Specifically, recordings with an SNR below 3.5 dB were excluded, as low SNRs increase the likelihood of spike misidentification.

Out of the 19 available recordings, five were excluded based on the SNR criterion (see supplemental figures). For the remaining 14 recordings with satisfactory SNR, the decomposition process started by segmenting the 252-channel probe into subgroups of approximately 36 channels, focusing on the sub-group closest to the patched source (identified by the 'best channel' in the database). The algorithm was initially run on the first 120 s of data, and the observation matrix was extended by a factor of 10 ($K = 10$, empirically determined). Each extracted source was compared to the ground-truth spike times, and if the error rate was below 20%, the algorithm ceased. In all cases, the peeling-off procedure was not required.

After successfully identifying the sources for the initial 120 s, the decomposition was extended to the entire recording length, which ranged from 180 s to 300 s. A manual visual inspection of the loose patch data was performed, during which threshold levels were adjusted as needed to correct misclassified spikes in the ground-truth.

2.2.2. In vivo *Neuropixel recording in mouse*

To evaluate the performance of NeuroNella on a dense *in vivo* dataset, we utilized a publicly available Neuropixel recording database [31]. This dataset involved recordings from an awake, head-fixed mouse, where a 'Phase 3' Neuropixel probe with 374 electrodes was inserted into the posterior brain region [7]. Neural activity was captured across multiple areas, including the visual cortex, hippocampus, and selected thalamic areas, covering a span of 3.8 mm of brain tissue. The signals were sampled at 30 kHz and pre-processed with a high-pass filter having a cutoff frequency of 300 Hz.

NeuroNella was applied to the first 60 s of the Neuropixel recording. To facilitate decomposition, the probe was segmented into 19 sub-groups with approximately 20 channels each. The extension factor was set for each subgroup as the ceiling integer that yielded an extended observation matrix of 300 virtual

channels (extension factor multiplied by the number of channels). For the decomposition process, the number of iterations set to both the original and peeled-off signals was 50, enabling NeuroNella to identify up to 100 sources per subgroup.

2.2.3. In vivo *recording in macaque*

A further dataset acquired in our laboratories (Baker laboratory, Newcastle University) was analyzed. This was recorded from the medullary reticular formation in a terminally anaesthetized female macaque monkey. This provided the opportunity to test the algorithm on sub-cortical recordings in a primate, in a region known to have multiple cell types [32]. The study complied with UK Home Office regulations. It was performed under personal and project licenses issued by the Home Office and was approved by the Animal Welfare and Ethical Review Board of Newcastle University. Under inhalation anaesthesia (1%–2% sevoflurane), a craniotomy was made in the skull adjacent to the foramen magnum, and a laminectomy made of the cervical spinal cord. The head was then fixed in a stereotaxic frame, angled down at 65°; the spinal cord was clamped using spinal clamps to be approximately horizontal. Anaesthesia was then switched to an intravenous infusion of ketamine (6 mg kg h^{-1}), alfentanil (0.2–0.3 μg kg min^{-1}) and midazolam (0.14 mg kg h^{-1}) [33], which we have found to provide a stable anaesthetic plane whilst maintaining neuronal activity. Anaesthetic monitoring throughout included heart rate, pulse oximetry, continual invasive arterial blood pressure, core and peripheral temperature, and capnography. Rapid rises in heart rate or blood pressure, or more gradual rising trends were taken as evidence of waning anaesthesia and additional bolus doses were given. The animal was kept warm with a thermostatically controlled heating blanket and a supply of warmed air. A continual fluid infusion was given to ensure hydration (total rate including drug infusions 5–10 ml kg h^{-1}). The cisterna magna was opened to visualize the obex. Recordings were made with a silicon probe electrode (poly3, Neuronexus Inc, Ann Arbor, MI, USA) which had 32 contacts (diameter 15 μm) arranged in three columns, with interelectrode spacing 25 μm and total length of the recording array 290 μm (see [34] for an image of the array layout). The electrode was held in a stereotaxic manipulator angled rostrally at 35° relative to the vertical line perpendicular to the spinal cord. The electrode tip was first zeroed to the obex landmark and was then moved to penetrate the brainstem 2 mm rostral, 1 mm lateral to obex. Recordings were made at a penetration depth of 8.2 mm below the depth measured at obex, which should lie within the *nucleus gigantocellularis*. Signals from all 32 channels were captured using an Intan RHD2132 headstage amplifier and associated USB interface (Intan Technologies Inc, Los Angeles, CA, USA), with sampling rate of 25 kHz and bandpass 1 Hz–10 kHz. For the reticular formation recording, we decomposed the first 60 s of data for the single segment comprising 32 channels. The extension factor was 12 and the number of iterations was 40 for each step of the decomposition. The decomposition was then extended for the first 20 min of recording following the procedures described in the section 'Extension of the Decomposition'.

2.3. Data analysis

For each extracted source, we obtained the spike waveform at all channels, with spike-triggered averaging, and the activation map, computed as the peak-to-peak amplitude of the spike waveforms for each channel. We also estimated the spike train of each source at each channel by convolving the spike waveforms with the discharge times. The residual signal was then obtained by subtracting the reconstructed spike trains from the original data. The residual energy was found as the root-mean square of the residual signal.

In order to quantify accuracy and precision in the identification of discharge instants, we computed the variance ratio (VR) of the action potential waveform (equation (1)) [35]. The VR was estimated for the spike waveforms triggered by the discharge instants at the extracellular recording closest to the source (largest spike amplitude)

$$\mathrm{VR} = \frac{\frac{\sum_{t=1}^{T}\sum_{n=1}^{N}(y_{t,n}-\bar{y}_t)^2}{T(N-1)}}{\frac{\sum_{t=1}^{T}\sum_{n=1}^{N}(y_{t,n}-\hat{y})^2}{TN-1}} \tag{14}$$

where T is the number of time points, N is the number of discharges, $y_{t,n}$ is the value of the nth discharge at time point t, $\bar{y}_t$ is the spike waveform value at time point t, averaged over the N discharges, and $\hat{y}$ is the grand mean.

To assess the performance of NeuroNella, we estimated the Error Rate of the extracted sources in comparison to the ground-truth sources. The error rate was computed by counting the number of false-positive and -negative discharges and dividing it by the total number of discharges from both sources. A tolerance of 0.5 ms of deviation was considered acceptable in the analysis.

For the Neuropixel sources, we first matched all source identified with NeuroNella to the sources provided in the database. Sources were considered matched if the cross-correlation between spike trains was higher than 0.5. We only analyzed sources with at least 10 discharges in the 60 s segment. Instead of error rates, we compared the discharge times of the NeuroNella and spike sorting matched sources by the rate-of-agreement (RoA), as follows:

$$\mathrm{RoA}_j = \frac{C_j}{C_j + N_j + S_j} 100\% \tag{15}$$

where C_j denotes the number of discharges of the jth source identified by both methods, and $[N_j, S_j]$

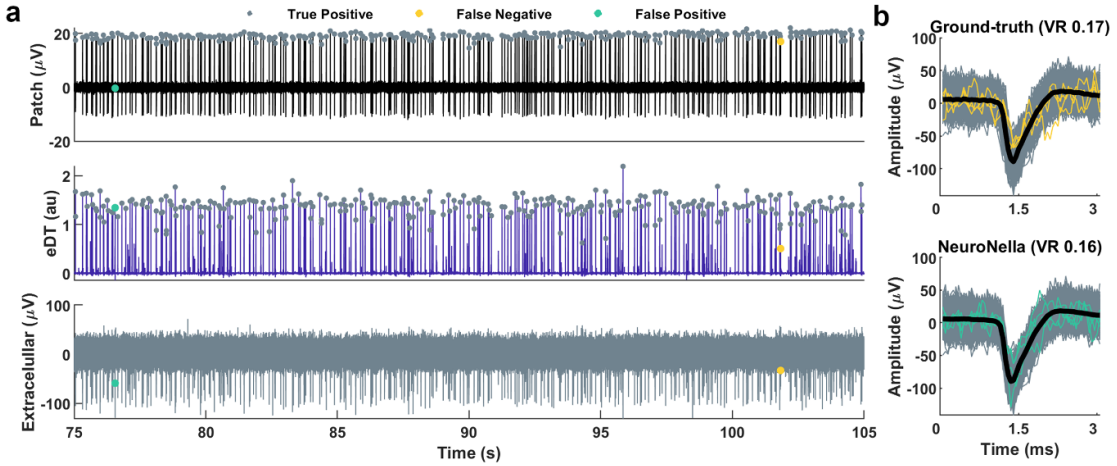

Figure 2. Representative comparison of the ground-truth discharge times and NeuroNella decomposition. (a) The patch signal (in black), the estimated discharge train (eDT) decomposed from the extracellular recordings with NeuroNella (in blue) and the best extracellular channel (with the largest spike amplitude, in gray) are shown for one source. Only 30 s are provided. (b) Shimmer plots for the best extracellular channel triggered by the ground-truth time instants (on the top) and triggered by the time instants detected by the decomposition algorithm (on the bottom). False-negative discharges (classified in the ground-truth data but not classified with NeuroNella) are depicted in yellow and false-positive discharges (not classified in the ground-truth but classified with NeuroNella) are depicted in green. The title contains the variance ratio (VR) of the shimmer plots.

are the number of discharges identified only by NeuroNella or spike sorted methods, respectively. The discharge time tolerance was 0.5 ms.

3. Results

3.1. Performance on ground-truth data

The average time to decompose each source for the initial 60 s segment of data was 141.59 ± 50.42 s (mean ± confidence interval, 14 recordings). The decomposition result for a representative recording is presented in figure 2. The discharge trains estimated with NeuroNella from the dense extracellular recording closely followed the patch signals. To quantify the performance of the algorithm, we estimated the error rate with respect to the ground-truth discharges. A representative false-positive is shown around time 76 s and a false-negative around time 102 s (figure 2(a)). Figure 2(b) shows the shimmer plots of the extracellular signal closest to the source triggered by the ground-truth and the discharge instants identified with NeuroNella.

NeuroNella achieved an averaged error rate of 0.42 ± 0.51% (figure 3(a)), which is significantly smaller than a recent spike sorting toolbox [8] that showed an averaged error rate of 5% on the same dataset. Even though a negative exponential correlation ($R^2 = 0.83$) was observed between the error rates and the peak-to-peak amplitude of the action potential, similar to the spike sorting-based algorithms [8], NeuroNella showcased superior performance across the entire amplitude range. This indicates that NeuroNella could automatically identify sources as small as 50 μV with a very low error rate. The PNR exceeded 30 dB for all estimated discharge trains (figure 3(b)).

Comparatively, NeuroNella exhibited a slightly smaller VR than the ground-truth (figure 3(c)), suggesting a precise selection of the discharge instants. The shimmer plots in figure 3(c) demonstrate the variances within the spike waveforms. It is important to acknowledge that the ground-truth instants were derived from the loose patch signal, leading to slight misalignments during the triggering of the extracellular recordings, thus resulting in a slightly greater VR. Additionally, figure 3(d) showcases instances of false-positive and false-negative spikes. Interestingly, some false-negative spikes (in green) closely resemble the averaged waveform (in black), while certain false-positives spikes (in yellow) appeared flat. These observations suggest potential misclassifications within the ground-truth instants rather than errors of NeuroNella. Specifically, in two recordings, the patch signal experienced drift and exhibited a dip in amplitude, resulting in errors during the classification of the discharge instants (see supplemental figures).

3.2. Performance on Neuropixel data

We also tested NeuroNella on an online database that involved the use of a Neuropixel probe featuring 374 electrodes (figure 4(a)). To facilitate decomposition, we segmented the probe into 19 subgroups, each consisting of approximately 20 channels (figure 4(b)). In total, we identified 292 neurons using NeuroNella, a lower number compared to the 492 sources provided in the dataset, which were identified by a spike sorting algorithm. Figure 5(b) reveals that the most significant disparities in source numbers were observed within segments displaying high energy. Nevertheless, the residual energy, measured as the root-mean-square difference between the

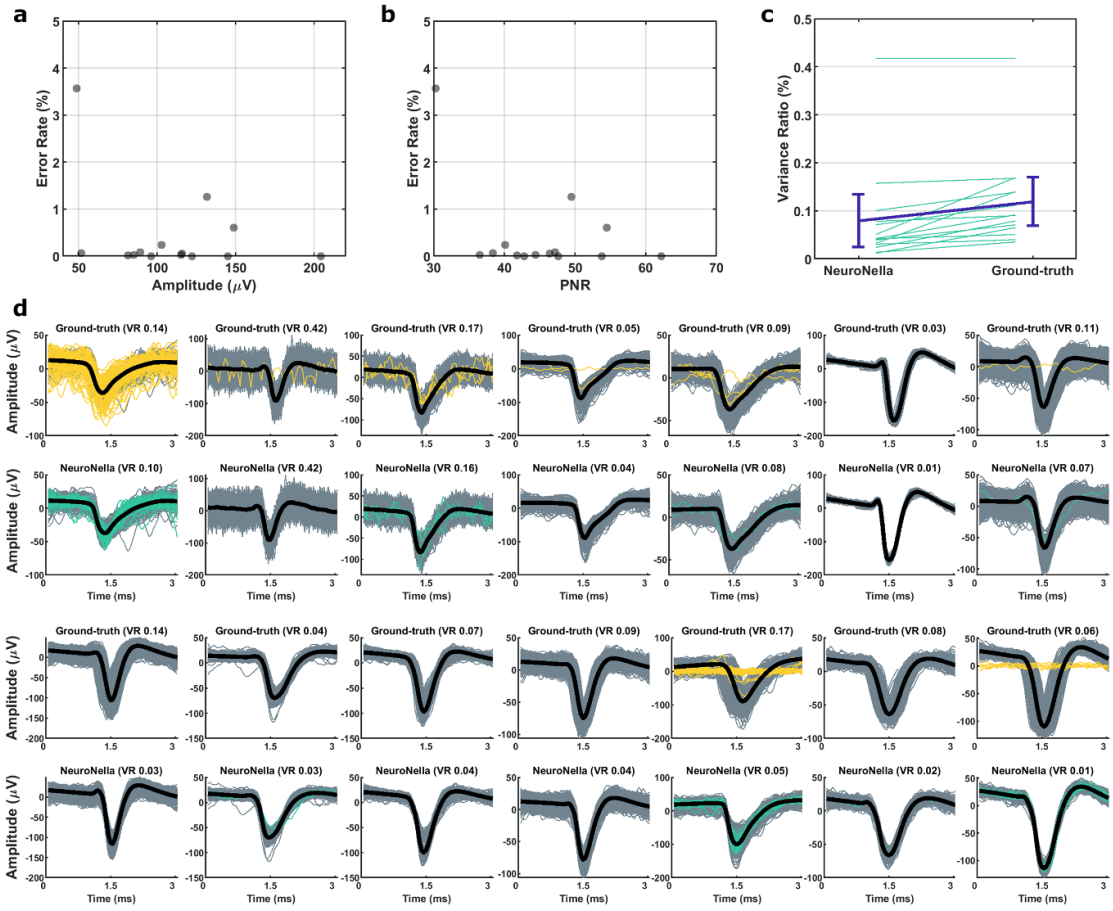

Figure 3. Error rate of the algorithm as a function of (a) the peak-to-peak amplitude of the decomposed source and (b) pulse-to-noise ratio (PNR) of the estimated discharge trains. Each circle represents one recording (N = 14). (c) Variance ratio of the spike waveforms triggered by the original ground-truth and the discharge instants identified with NeuroNella at the extracellular recording closest to the sources. (d) Shimmer plots of the extracellular recordings triggered by the ground-truth (first and third rows) and NeuroNella discharge instants (second and fourth rows) for the 14 recordings. False-negatives and false-positives instants are depicted in yellow and green, respectively. True positives are depicted in gray, while the averaged waveform is in shown in black. The variance ratio (VR) of each shimmer plot is presented in the title.

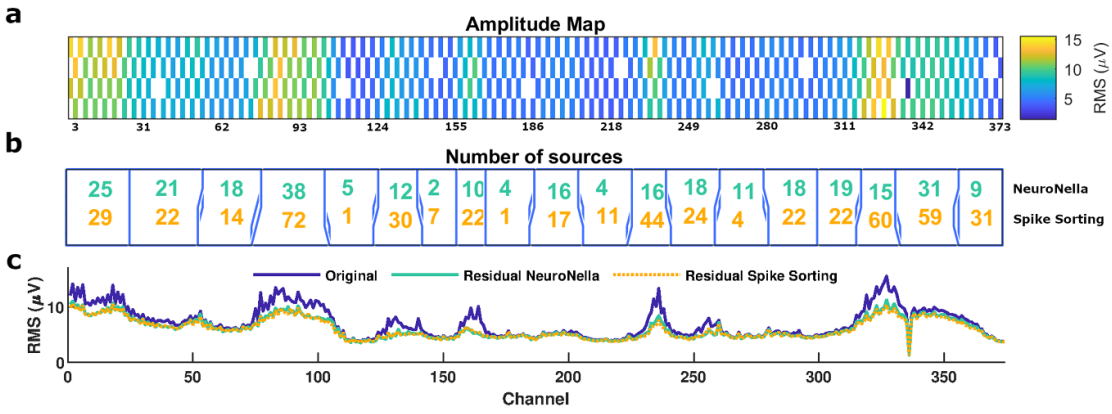

Figure 4. (a) Amplitude map with the signal energy (root-mean-squared—colored-coded) for a 60 s duration dataset recorded with a Neuropixel probe (374 electrodes). (b) Number of sources identified with NeuroNella (green) and spike sorting algorithm (orange) for each sub-group (blue polygons). (c) Residual energy for NeuroNella (green) and spike sorting (orange) algorithms compared to the original signal energy (blue) for each electrode.

original signal and the signal reconstructed from the identified neuron, exhibited only relatively minor differences between the two methods (figure 4(c)). In fact, the residual energy approached the noise level (<7 μV, as indicated in the database) for most electrodes. Notably, the total number of discharges identified by NeuroNella exceeded that reported by the database, with 239 081 spikes against 232 071. This

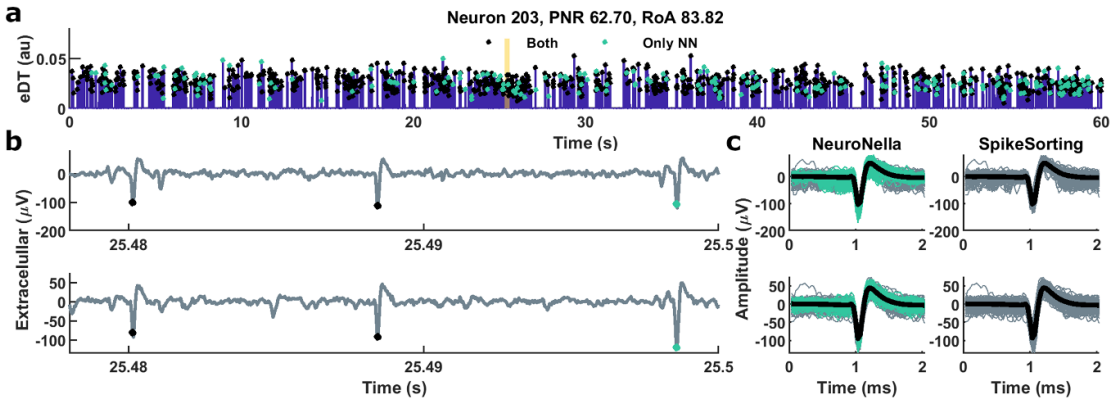

Figure 5. Representative comparison of the NeuroNella decomposition and the provided matched source identified by a spike sorting-based algorithm. (a) The estimated discharge train (eDT) decomposed with NeuroNella (in blue) for the initial 60 s of recording. Discharge instants detected by both methods are indicated by black markers, while those exclusively identified by NeuroNella are marked in green. (b) Zoomed-in views of the two largest-amplitude extracellular recordings aligned with the orange line in the eDT. (c) Shimmer plots for the corresponding extracellular channels triggered by NeuroNella (on the left) and by the spike sorting time instants (on the right). Spikes classified solely by NeuroNella are depicted in green. The figure title contains the source number, the pulse-to-noise ratio (PNR) of the eDT and the Rate-of-Agreement (RoA) of the classification methods.

finding suggests that the disparity in the number of sources compared to the dataset might be attributed to the possibility that NeuroNella may have merged certain sources or that the dataset segmented some sources differently. To illustrate this further, figure 5 presents a high-quality source (PNR = 62.7 dB) identified by NeuroNella. This source had an 84% RoA with one source from the dataset and 5% RoA with a second source. The close resemblance of the spike waveforms identified solely by NeuroNella to the averaged waveform (figure 5(c)) strongly suggests potential misclassification of these discharges within the dataset.

A total of 184 NeuroNella sources were matched to the sources provided in the database. The dataset also categorized the sources as either 'good single unit' or 'multiple unit'. NeuroNella identified 144 out of 223 (65%) 'good single unit', and 40 out of 269 (15%) 'multiple units'. The peak-to-peak amplitude of the 'single units' matched sources ranged from 18 μV to 280 μV (figure 6(a)). The sources recognized by only one method are also shown in figure 6(a).

There was a correlation between the metric of quality of the blind source separation algorithm (PNR) and the amplitude of the source (figure 6(b)). Notably, most of the sources that were not matched to the dataset exhibited small amplitudes, which can also be seen in figure 6(a). For the sources that matched, the RoA varied significantly when the decomposition quality was below 50 dB; in contrast, the RoA was 97.25 $\pm$ 1.49% (mean $\pm$ confidence interval) for sources with PNR above 50 dB (figure 6(c)). Figure 6(d) shows the difference between the VR of the matched sources for the spike's waveforms triggered by NeuroNella and spike sorting instants. The variance ratio was observed to be smaller for NeuroNella than for spike sorting (median variance ratio of 0.19 vs 0.21, respectively), signifying a more precise classification.

3.3. Collected dataset in the reticular formation

We found 26 sources on our own recordings from the ponto-medullary reticular formation in an anaesthetized macaque (figure 7(a)). The energy for the residual signals reached the noise level, indicating that the most significant sources were identified (figure 7(b)). The variance ratio was below 0.5% for all sources and was negatively correlated with the PNR ($p = 0.014$, $R^2 = 0.22$, figure 7(c)).

We then extended the decomposition to 20 min and found 10 neurons constantly active. Notably, the discharge identification for the extended decomposition was robust to recording instability, as shown by drifts in the amplitude of the extracellular signals (figure 8(a)) and changes in the action potential waveforms with time (figure 8(b)).

4. Discussion

We developed a method that leverages the sparsity of the action potentials from multichannel electrode arrays implanted in different locations in the nervous system of mice, rats, and monkeys. NeuroNella showed high reliability in identifying the same spike even in cases of overlapping action potentials. We found matching accuracy between the loose patch and multichannel extracellular action potentials close to 100%. The spike times of the neurons were identified in a fully automatic way, therefore, opening new avenues not only for offline processing in basic and applied neuroscience research but also for future online use in brain/machine interfaces.

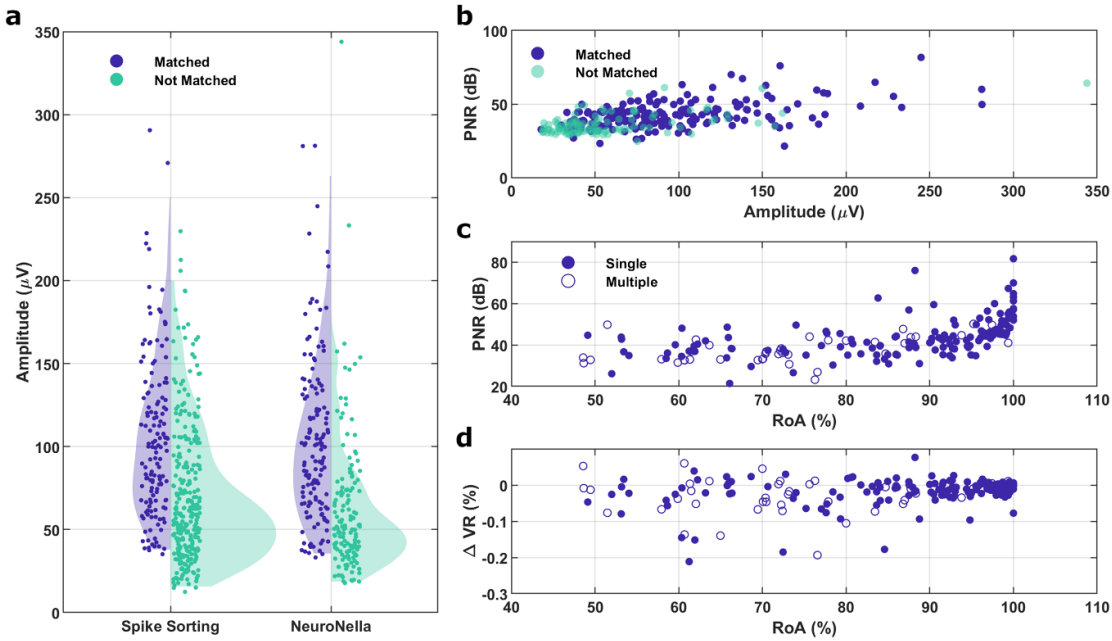

Figure 6. (a) Peak-to-peak amplitude of the population identified with spike sorting and NeuroNella methods. Sources found by both methods (matched) are in blue and sources found by only one method are in green. (b) Pulse-to-noise ratio (PNR) of the estimated discharge train in relation to the peak-to-peak amplitude of the spike waveform. (c) PNR in relation to the rate of agreement (RoA) of the spike instants for the matched sources classified as 'Single Unit' (filled circles) or 'Multiple Units' (open circles). (d) Difference between the variance ratio of the spike waveforms triggered by the discharge instants identified by NeuroNella and spike sorting algorithms in relation to the RoA.

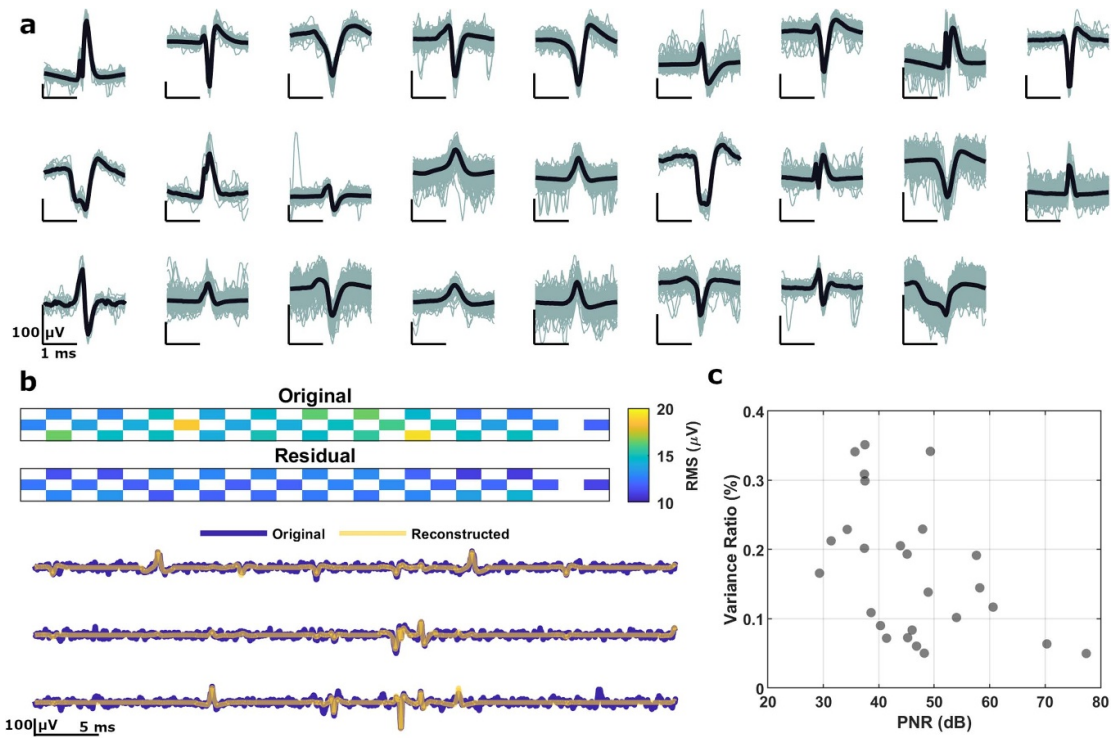

Figure 7. (a) Shimmer plot of 26 sources identified with NeuroNella in an extracellular recording of the reticular formation. (b) Amplitude map with the signal energy (root-mean-squared—colored-coded) for a 60-s duration dataset recorded with a linear U probe with 32–electrodes, and the residual energy for comparison. Bellow, representative signals recorded in three electrodes (blue) and the respective reconstructed signals from the identified neurons (yellow). (c) Variance ratio as a function of the pulse-to-noise ratio (PNR) of the estimated discharge train.

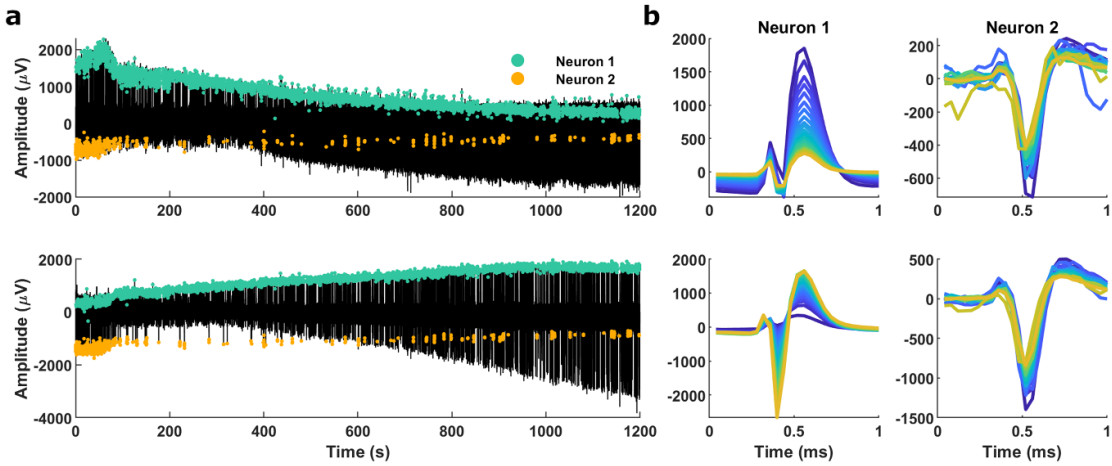

Figure 8. Representative results for the decomposition of a 20 min recording. (a) Two extracellular signals displaying the discharge instances identified for two neurons (green and orange markers). (b) Action potential waveforms corresponding to Neuron 1 (on the left) and Neuron 2 (on the right) for the respective extracellular signals estimated at every minute of recording.

The automated decomposition and extension processes demonstrate remarkable efficacy in detecting sources of varying amplitudes, exhibiting an exceptional level of accuracy. We observed that error rates >0.5% were predominantly associated with the challenges of peak identification within the estimated discharge train and the loose patch signal. In figure 3, numerous supposedly false-negative discharges do not resemble the action potential waveform, while the supposedly false-positives did, possibly underscoring the impact of utilizing a simplistic amplitude threshold for identifying discharge instants within the loose patch signals. Beyond the identification of discharge instances, the quality of the ground-truth signal emerged as a more crucial factor. In this dataset, four recordings were excluded due to low SNR. These recordings exhibited not only elevated noise levels but also significant variance ratio in the discharge amplitude (see Supplemental Figures). Such variability likely reflects suboptimal attachment of the loose patch to the cell. This reinforces the importance of ensuring high-quality ground-truth signals to support accurate analysis and reliable algorithm performance [29].

Through our analysis, we found that adopting a more rigorous approach favoring decompositions with a PNR exceeding 50 dB guarantees the overall reliability of our results. The PNR index, as defined in this study by equation (9), derives from the PNR index of the decomposition of HD-sEMG into motor units spike trains [25]. For the later application, the threshold is usually set to 30 dB, as it provides sensitivity higher than 90% and errors below 2% [25]. In this study, the PNR values and the recommended threshold are notably higher due to a distinct calculation method—employing a power of three instead of the power of two used in the electromyogram, which further nonlinearly amplifies the peaks over the noise. In instances where the estimated discharge trains exhibit a low PNR, typically associated with sources characterized by small amplitudes, close proximity to other active sources, or limitations in the spatial resolution of the acquisition system, we strongly recommend a manual inspection with the semi-automatic classification algorithm (figure 1(b)). This algorithm is specially designed to consider the distinctive waveform characteristics of each spike across neighboring electrodes to classify the peaks identified in the estimated discharge train properly.

A critical step in the NeuroNella decomposition involve segmenting the probe into smaller subgroups of electrodes. However, this segmentation process did not consider the spatial distribution of individual sources; instead, it relied on overall signal energy, potentially resulting in suboptimal segmentation regarding the selectivity of individual sources. Despite this, the decomposition process proved effective, highlighting its resilience even with incomplete spatial information. A follow-on study may evaluate if probe segmentation based on detected neuronal activities increases the number of identified sources and improve the overall quality of the decomposition.

Results indicate that the comparatively lower number of sources identified by NeuroNella appears to be more closely associated with the intricacies of spike identification rather than a fundamental limitation of the Blind Source Separation algorithm in detecting some sources. Several key observations support this hypothesis. In figure 6, NeuroNella successfully detected sources within the same amplitude range as the spike sorting provided with the online dataset. Additionally, figure 5 illustrates possible misclassifications by that spike sorting algorithm, suggesting subdivision of sources in the dataset. Finally, figure 6(d) exhibited a lower variance ratio of the spikes when triggered by the NeuroNella discharge times compared with the times provided in

the dataset. Notably, considering a minimal 0.03% difference between the variance ratio of matched sources, NeuroNella displayed lower values for 90% of the sources. This suggests that it is more likely that spike sorting missed spikes (or split sources) rather than that NeuroNella falsely selected pulses (or merged sources), since otherwise the variance ratio would have been higher. These misclassification cases became particularly evident in decompositions characterized by a high PNR and a low RoA. Therefore, sources featuring PNR values above 40 dB and with RoAs ranging between 60% and 90% in figure 6(b) likely resulted from erroneous classifications by the spike sorting algorithm.

In addition to the potential misclassifications, it is important to highlight that the unmatched sources in the online dataset were predominantly classified as 'multiple units', which might not hold significant relevance for many research studies. NeuroNella seemed to prioritize the automatic identification of 'good single units', which will ensure a more focused and relevant dataset for further analysis.

Our investigation further demonstrated that the NeuroNella algorithm effectively extended the decomposition process to large datasets (30 min). Results showed high robustness of the extended decomposition process in handling minor probe shifts (figure 8). This resilience underscores the potential application in longitudinal studies and prolonged recordings sessions. Moreover, the algorithm holds promise for online decomposition as it is based on a simple multiplication of the separation vector (identified in an offline step) and the new data. The process follows the same principle of online decomposition of HD-sEMG [28, 36]. However, it is important to note that this process only guarantees precision for the high-energy sources, and not for smaller sources identified after the peel-off procedure.

5. Conclusion

NeuroNella has proven to be a highly effective and efficient algorithm for identifying neuronal activity from multielectrode arrays. Its high accuracy, capacity to handle large datasets, and resilience to minor probe shifts underscore its utility in various applications. These capabilities open promising avenues for real-time neuronal decoding system and advanced neurological research.

Data availability statement

All data that support the findings of this study are included within the article (and any supplementary files) [37, 38].

Acknowledgments

CG acknowledges Fundação de Amparo à Ciência e Tecnologia do Estado de Pernambuco (FACEPE) (Grant number APQ-0080-3.13/23) and São Paulo Research Foundation (FAPESP) (Grant number 2024/08318-4). AV acknowledges Bavarian Ministry of Economic Affairs, Regional Development and Energy (StMWi) (Grant number MV-2303-0006), European Research Council (ERC) (Grant number 101118089), and German Federal Ministry of Education and Research (BMBF) (Grant number 01DN23002). DF acknowledges Engineering and Physical Sciences Research Council (EPSRC) (Grant number EP/T020970/1). SB and DF acknowledge Biotechnology and Biological Sciences Research Council (BBRSC) (Grant Number BB/V00896X/1).

Ethical Statement

Experiments in macaque were approved by the Animal Welfare and Ethical Review Board of Newcastle University and conducted under appropriate personal and project licences from the UK Home Office.

ORCID iDs

C Germer https://orcid.org/0000-0002-7323-3767
D Farina https://orcid.org/0000-0002-7883-2697
S N Baker https://orcid.org/0000-0001-8118-4048
A Del Vecchio https://orcid.org/0000-0002-7118-5554

References

[1] Adrian E D and Bronk D W 1929 The discharge of impulses in motor nerve fibres *J. Physiol.* **67**
[2] Velliste M, Perel S, Spalding M C, Whitford A S and Schwartz A B 2008 Cortical control of a prosthetic arm for self-feeding *Nature* **453** 1098–101
[3] Collinger J L, Boninger M L, Bruns T M, Curley K, Wang W and Weber D J 2013 Functional priorities, assistive technology, and brain-computer interfaces after spinal cord injury *J. Rehabil. Res. Dev.* **50** 145–60
[4] Collinger J L, Wodlinger B, Downey J E, Wang W, Tyler-Kabara E C, Weber D J, McMorland A J C, Velliste M, Boninger M L and Schwartz A B 2013 High-performance neuroprosthetic control by an individual with tetraplegia *Lancet* **381** 557–64
[5] Donoghue J P 2002 Connecting cortex to machines: recent advances in brain interfaces *Nat. Neurosci.* **5** 1085–8
[6] Angotzi G N, Boi F, Lecomte A, Miele E, Malerba M, Zucca S, Casile A and Berdondini L 2019 SiNAPS: an implantable active pixel sensor CMOS-probe for simultaneous large-scale neural recordings *Biosens. Bioelectron.* **126** 355–64
[7] Jun J J *et al* 2017 Fully integrated silicon probes for high-density recording of neural activity *Nature* **551** 232–6
[8] Yger P *et al* 2018 A spike sorting toolbox for up to thousands of electrodes validated with ground truth recordings in vitro and in vivo *Elife* **7** 1–23

[9] Saif-Ur-Rehman M et al 2021 SpikeDeep-classifier: a deep-learning based fully automatic offline spike sorting algorithm J. Neural Eng. 18 016009
[10] van der Molen T et al 2024 RT-Sort: an action potential propagationbased algorithm for real time spike detection and sorting with millisecond latencies PLoS One 19 e0312438
[11] Hilgen G et al 2017 Unsupervised spike sorting for large-scale, high-density multielectrode arrays Cell Rep. 18 2521–32
[12] Meyer L M, Zamani M, Rokai J and Demosthenous A 2024 Deep learning-based spike sorting: a survey J. Neural Eng. 21 061003
[13] Buccino A P, Garcia S and Yger P 2022 Spike sorting: new trends and challenges of the era of high-density probes Prog. Biomed. Eng. 4 022005
[14] Bankman I N, Johnson K O and Schneider W 1993 Optimal detection, classification, and superposition resolution in neural waveform recordings IEEE Trans. Biomed. Eng. 40 836–41
[15] Jäckel D, Frey U, Fiscella M and Hierlemann A 2011 Blind source separation for spike sorting of high density microelectrode array recordings 2011 5th Int. IEEE/EMBS Conf. on Neural Engineering, NER 2011 pp 5–8
[16] Farina D and Holobar A 2016 Characterization of human motor units from surface EMG decomposition Proc. IEEE 104 353–73
[17] Holobar A and Zazula D 2007 Multichannel blind source separation using convolution Kernel compensation IEEE Trans. Signal Process. 55 4487–96
[18] Negro F, Muceli S, Castronovo A M, Holobar A and Farina D 2016 Multi-channel intramuscular and surface EMG decomposition by convolutive blind source separation J. Neural Eng. 13 026027
[19] Chen M, Zhang X, Chen X and Zhou P 2018 Automatic implementation of progressive FastICA peel-off for high density surface EMG decomposition IEEE Trans. Neural Syst. Rehabil. Eng. 26 144–52
[20] Buchner H, Aichner R and Kellermann W 2004 Blind source separation for convolutive mixtures: a unified treatment Audio Signal Processing for Next-Generation Multimedia Communication Systems ed Huang Y and Benesty J (Springer) pp 255–93
[21] Pedersen M S, Larsen J, Kjems U and Parra L C 2008 Convolutive blind source separation methods Springer Handbook of Speech (Springer) pp 1065–94
[22] Hyvarinen A, Karhunen J and Oja E 2001 Independent Component Analysis (Wiley)
[23] Hyvärinen A and Oja E 1997 A fast fixed-point algorithm for independent component analysis Neural Comput. 9 1483–92
[24] Hyvärinen A 1999 Fast and robust fixed-point algorithms for independent component analysis IEEE Trans. Neural Netw. 10 626–34
[25] Holobar A, Minetto M A and Farina D 2014 Accurate identification of motor unit discharge patterns from high-density surface EMG and validation with a novel signal-based performance metric J. Neural Eng. 11 016008
[26] Mitianoudis N, Stathaki T and Davies M 2005 Blind separation of skewed signals in instantaneous mixtures IEEE Workshop on Signal Processing Systems, SiPS: Design and Implementation vol 2005 pp 407–12
[27] Chen M and Zhou P 2016 A novel framework based on FastICA for high density surface EMG decomposition IEEE Trans Neural Syst Rehabil Eng. 117–27
[28] Chen C, Ma S, Sheng X, Farina D and Zhu X 2020 Adaptive real-time identification of motor unit discharges from non-stationary high-density surface electromyographic signals IEEE Trans. Biomed. Eng. 9294 1
[29] Spampinato G L, Esposito E, Yger P, Duebel J, Picaud S and Marre O 2018 Ground truth recordings for validation of spike sorting algorithms Zenodo (https://doi.org/10.5281/zenodo.1205232)
[30] Disselhorst-Klug C, Silny J and Rau G 1997 Improvement of spatial resolution in surface-EMG: a theoretical and experimental comparison of different spatial filters IEEE Trans. Biomed. Eng. 44 567–74
[31] Steinmetz N A and Matteo Carandini Kenneth Harris 2024 Simultaneous recording with two Neuropixels probes University College London. Dataset. (https://doi.org/10.5522/04/25226867.v1)
[32] Zaaimi B, Soteropoulos D S, Fisher K M, Riddle C N and Baker S N 2018 Classification of neurons in the primate reticular formation and changes after recovery from pyramidal tract lesion J. Neurosci. 38 6190–206
[33] Fisher K M, Zaaimi B, Edgley S A and Baker S N 2021 Extensive cortical convergence to primate reticulospinal pathways J. Neurosci. 41 1005–18
[34] Kraskov A, Soteropoulos D S, Glover I S, Lemon R N and Baker S N 2020 Slowly-conducting pyramidal tract neurons in macaque and rat Cereb. Cortex 30 3403–18
[35] Kumar R I, Mallette M M, Cheung S S, Stashuk D W and Gabriel D A 2020 A method for editing motor unit potential trains obtained by decomposition of surface electromyographic signals J. Electromyogr. Kinesiol. 50 102383
[36] Wen Y, Avrillon S, Hernandez-Pavon J C, Kim S J, Hug F and Pons J L 2021 A convolutional neural network to identify motor units from high-density surface electromyography signals in real time J. Neural Eng. 18 056003
[37] Germer C, Farina D, Baker S and Del Vecchio A 2024 Identification of Neuronal Activity from Extracelullar Recordings with Ground-truth Patch Clamp Code for In Vitro Ground-Truth Decomposition: Germer (https://doi.org/10.6084/m9.figshare.25979281)
[38] Germer C, Baker S, Farina D and Del Vecchio A 2025 NeuroNella Dataset: Multielectrode Array Decomposition for Neuronal Activity (https://doi.org/10.6084/m9.figshare.28706408.v1)